nature nanotechnology

Article

https://doi.org/10.1038/s41565-026-02134-z

Magnetic circular dichroism imaging of atomic-scale antiferromagnetic order at a buried interface

Received: 30 July 2025

Accepted: 20 January 2026

Published online: 23 March 2026

Check for updates

Dongsheng Song[1,2] ✉, Fengshan Zheng[2,3], Lin Hao[4], Lei Jin[2], Yajiao Ke[5], Yizhou Liu[4], Mingliang Tian[4,6], Binghui Ge[1], Rafal E. Dunin-Borkowski[2] & Haifeng Du[4] ✉

Magnetic circular dichroism utilizing electrons or X-rays serves as a powerful tool for the investigation of magnetism in ferromagnets, but antiferromagnets pose a severe challenge to the technique due to their vanishing net magnetization. Although transmission electron microscopy has demonstrated the atomic-scale characterization of antiferromagnetism using elastically scattered electrons, separating the weak magnetic signal from the dominant electrostatic background remains challenging, and applicability is largely limited to perfect crystals. Here we develop atomic-column-resolved electron magnetic circular dichroism to resolve antiferromagnetic order using a scanning transmission electron microscope. By exploiting chirality around individual magnetic atomic columns, we localize the magnetic circular dichroism signals around the transmitted electron beam with enhanced strength and signal-to-noise ratio, enabling atomic-column magnetic measurements. Applying this technique to antiferromagnets, we not only distinguish the characteristic G-type and C-type antiferromagnetic orderings in $DyFeO_3$ and α-Fe_2O_3 but also identify a one-unit-cell-thick magnetic dead layer at the buried $DyScO_3$–$SmFeO_3$ interface. Our work establishes a readily accessible method for atomic-scale magnetic order mapping, with potential applications in fields such as interfacial magnetism, topological magnetism, antiferromagnetism and altermagnetism.

X-ray magnetic circular dichroism (XMCD)[1,2] is a powerful synchrotron-based X-ray absorption spectroscopy technique used to probe ferromagnetism by exploiting circularly polarized X-rays. The XMCD signal originates from the excitation of core electrons into unoccupied conduction states, which requires an imbalance in the spin density of states in ferromagnets. Due to the absence of net spin polarization and magnetization, XMCD cannot directly measure antiferromagnetic materials. Nevertheless, this spin imbalance exists at the scale of individual atomic columns within antiferromagnets. Detecting such localized magnetic states could be possible—provided a sufficient spatial resolution is achieved. Yet, this remains beyond the reach of current X-ray spectroscopy techniques.

Aberration-corrected transmission electron microscopy (TEM) can form atomic-sized electron probes, enabling magnetic measurements at the atomic scale. When high-energy electrons travel through a magnetic crystal, they acquire both magnetic and electrostatic phase shifts[3]. Separating these contributions is challenging because the magnetic phase shift at atomic resolution is typically three orders of magnitude smaller

A full list of affiliations appears at the end of the paper. ✉e-mail: dsong@ahu.edu.cn; duhf@hmfl.ac.cn

https://doi.org/10.1038/s41565-026-02134-z

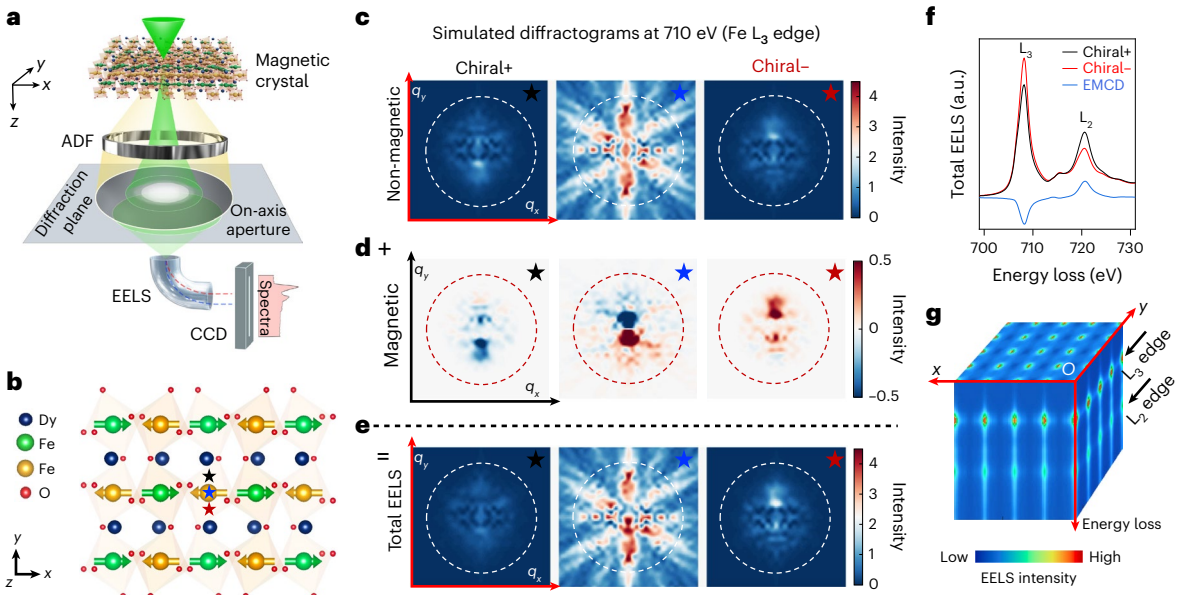

Fig. 1 | Principle of atomic-column EMCD imaging via STEM-EELS using transmitted electrons. a, Schematic of the STEM-EELS setup for antiferromagnet $DyFeO_3$ with a G-type spin configuration. The electron beam propagates along the *z* axis. The Néel vector is oriented along the *x* axis. An ADF detector captures an atomic-resolution image simultaneously with EELS acquisition. The diffraction pattern contains both non-magnetic and magnetic contributions. A post-column spectrometer records the EELS signals on a digital detector. CCD, charge-coupled device. **b**, Atomic model of $DyFeO_3$ projected along the *z* axis. Fe atoms (green and orange) have spin orientations along ±*x*. Stars mark three real-space electron probe positions. **c**–**e**, Simulated non-magnetic (**c**), magnetic (**d**) and total (**e**) signals in the diffraction plane at an energy loss of 710 eV for the three probe positions defined in **b**. The semiconvergence angle is 17.8 mrad and the sample thickness is 22.38 nm. Dashed circles denote the on-axis EELS entrance aperture. The diffraction plane extends over $q_x = \pm 40$ mrad and $q_y = \pm 40$ mrad. The integrated non-magnetic signal from the on-axis EELS aperture is identical for the two chiral positions (black and red stars), whereas the integrated magnetic signals are opposite in sign, giving rise to position-dependent chiral EELS signals. **f**, Schematic of the total chiral EELS signals in **e** from two chiral probe positions described in **b**, shown for the Fe $L_{3,2}$ edges. Their difference yields the EMCD signal for a single atomic column. **g**, Three-dimensional datacube obtained from the STEM-EELS experiment, with *x* and *y* representing the real-space scanning dimensions.

than the electrostatic phase shift. To address this, unique TEM facilities have been developed based on phase contrast techniques, including atomic-plane-resolved electron holography for the ferrimagnet Ba_2FeMoO_6 in an ultrahigh-voltage (1.2-MV) TEM with a pulsed magnetization system[4] and atomic-column-resolved differential phase contrast (DPC) imaging of antiferromagnetic α-Fe_2O_3 in a dedicated magnetic-field-free TEM[5]. These experimental constraints hinder broader application and largely confine the techniques to magnetic crystals, limiting their ability to characterize magnetism at defects.

Electron magnetic circular dichroism (EMCD)[6] measures ferromagnetism using inelastically scattered electrons based on electron energy-loss spectroscopy (EELS) in TEM. Analogous to XMCD, EMCD detects element-specific magnetic signals by comparing the EELS spectra at conjugate reciprocal-space positions, enabling the quantification of spin and orbital moments[7,8]. Despite its potential for the atomic-scale magnetic imaging of antiferromagnets, EMCD faces two main obstacles: low signal-to-noise ratio due to weak inelastic signals from an off-axis experimental setup[9] and spatial resolution that is limited to atomic planes by a three-beam diffraction geometry[10–12].

In this paper, we introduce an atomic-column-resolved EMCD technique implemented in a standard STEM-EELS[13–15] setup on a commercially available aberration-corrected scanning TEM (STEM). Our redesigned diffraction geometry preserves atomic-column resolution by operating on the zone axis and enhancing the signal intensity by an order of magnitude through on-axis acquisition compared with conventional off-axis setups. Applying this technique to antiferromagnets $DyFeO_3$ and α-Fe_2O_3, we resolve their distinct G-type and C-type antiferromangtic orderings at the atomic-column level. We further map the magnetic dead layer (MDL) at the buried $DyScO_3$–$SmFeO_3$ interface, revealing a one-unit-cell-thick region of suppressed magnetism as the antiferromagnetic coupling remains intact.

Principle of atomic-column EMCD

Figure 1a shows the experimental setup for atomic-column EMCD in a STEM. An atomic-sized electron probe passes through an antiferromagnetic crystal, in which inelastic scattering occurs as electrons interact with the magnetic atoms, exciting transitions such as those from 2*p* to unoccupied 3*d* orbitals at the Fe $L_{3,2}$ edge. In a standard STEM-EELS setup, an annular dark-field (ADF) detector is used to collect high-angle-scattered electrons to image atomic columns, whereas an EEL spectrometer records inelastic scattering signals simultaneously by using an on-axis EELS aperture in the diffraction plane to generate a spectrum on a digital detector. For a magnetic crystal, in which time-reversal symmetry is broken, the EELS signal contains both non-magnetic and magnetic (EMCD) components[16,17]. By analysing the distribution of these signals in the diffraction plane, the EMCD signals can be isolated.

Conventional EMCD signals are obtained under a three-beam geometry by measuring the off-axis chiral EELS signals at two conjugate positions in the diffraction plane[6], where the EMCD signals are dispersed across four quadrants with low intensity. Considering the chirality around individual magnetic atomic columns, which is absent in non-magnetic ones, EELS signals are also chiral across magnetic atoms and EMCD signals can be extracted in real space[18]. To verify this, we take the example of antiferromagnetic orthoferrite $DyFeO_3$, which has a G-type spin configuration (Fig. 1b). The Fe spins form a regular pattern of alternating magnetic ordering across the entire lattice[19]. The atomic model is projected along the *z* direction (zone-axis geometry) and the spins are oriented along the *x* axis. We placed the electron probe at two symmetrical positions around a magnetic atom column (Fig. 1b, stars). We then simulated the distribution of non-magnetic and magnetic signals in the diffraction plane (Fig. 1c–e). The dashed circle marks the position of the on-axis EELS entrance aperture used for signal acquisition.

https://doi.org/10.1038/s41565-026-02134-z

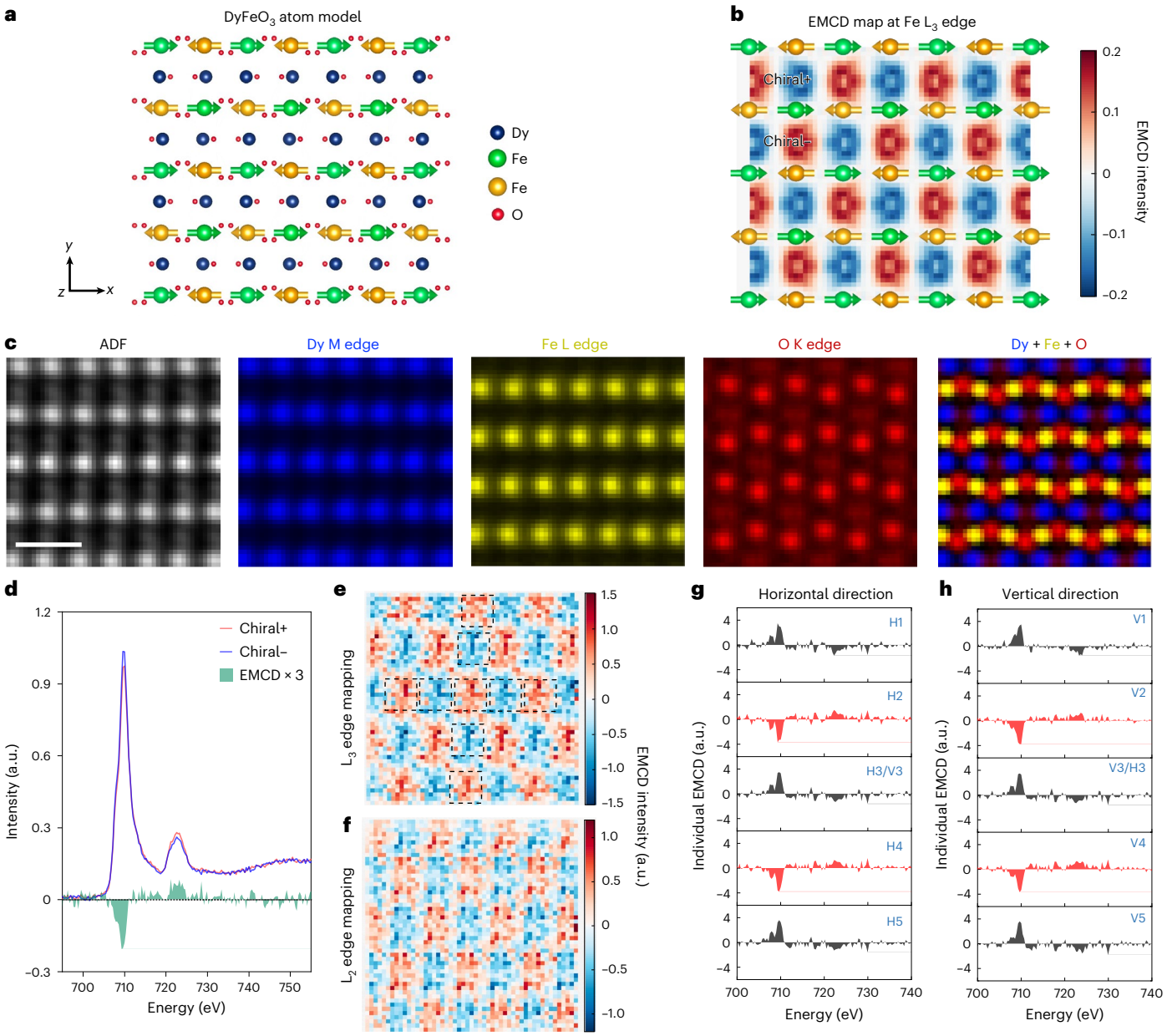

Fig. 2 | Atomic-column-resolved EMCD signals in the G-type antiferromagnet $DyFeO_3$. **a**, Atomic model of $DyFeO_3$ projected along the *z* axis, showing the spin orientations of the Fe atoms. **b**, Simulated real-space magnetic EMCD signals for the region shown in **a**. The Fe atomic model is overlaid to highlight the EMCD signal distribution, with the chiral+ and chiral− positions indicated. **c**, ADF image and elemental maps of Dy, Fe and O calculated from a STEM-EELS datacube after template-matching processing. The rightmost panel shows a combined elemental map. **d**, Averaged chiral EELS and EMCD signals obtained from the chiral+ and chiral− positions across the entire STEM-EELS datacube. **e**,**f**, L_3 (**e**) and L_2 (**f**) EMCD maps generated by integrating the EMCD signals at the $L_{3,2}$ edges. **g**,**h**, EMCD signals for individual atomic columns in the horizontal (**g**) and vertical (**h**) directions, corresponding to the dashed rectangles in **e**. Images in **c**, **e** and **f** have the same size. Scale bar, 5 Å.

When the electron probe is positioned on the centre of an atomic column (marked by a blue star), the EMCD signal distributions are antisymmetric in the diffraction plane, resulting in a net zero magnetic signal in the on-axis EELS aperture (Fig. 1d). At two symmetrical positions that are offset from the atomic column (marked by black and red stars), the non-magnetic signal is symmetric with respect to the centre of the diffraction plane (Fig. 1c), and the integrated signal in the aperture remains unchanged. By contrast, the magnetic signals are antisymmetric and the sign of the integrated signal is reversed (Fig. 1d). Therefore, the EMCD signals can be obtained by subtracting the total chiral EELS signals (Fig. 1e) from the two symmetrical positions around the magnetic atom columns, as schematically shown in Fig. 1f for the Fe $L_{3,2}$ edges. By using this approach, the entire magnetic lattice can be scanned to generate a three-dimensional datacube, in which the *x* and *y* axes are real-space positions (Fig. 1g). By extracting the EMCD signals from each atomic column, the magnetic ordering can be mapped with atomic-column lateral resolution. Note that the spins here are oriented perpendicular to the electron beam direction[18,20], unlike in conventional EMCD where they are parallel to the electron beam[6]. This configuration localizes the magnetic signal around the directly transmitted electron beam, enabling the use of an on-axis EELS acquisition setup and the enhancement of signal intensity (Supplementary Note 1 and Supplementary Fig. 1).

Imaging antiferromagnetic order in $DyFeO_3$

We simulated EMCD signals for G-type $DyFeO_3$ with atomic-column resolution (Methods) for an electron probe that was scanned across

https://doi.org/10.1038/s41565-026-02134-z

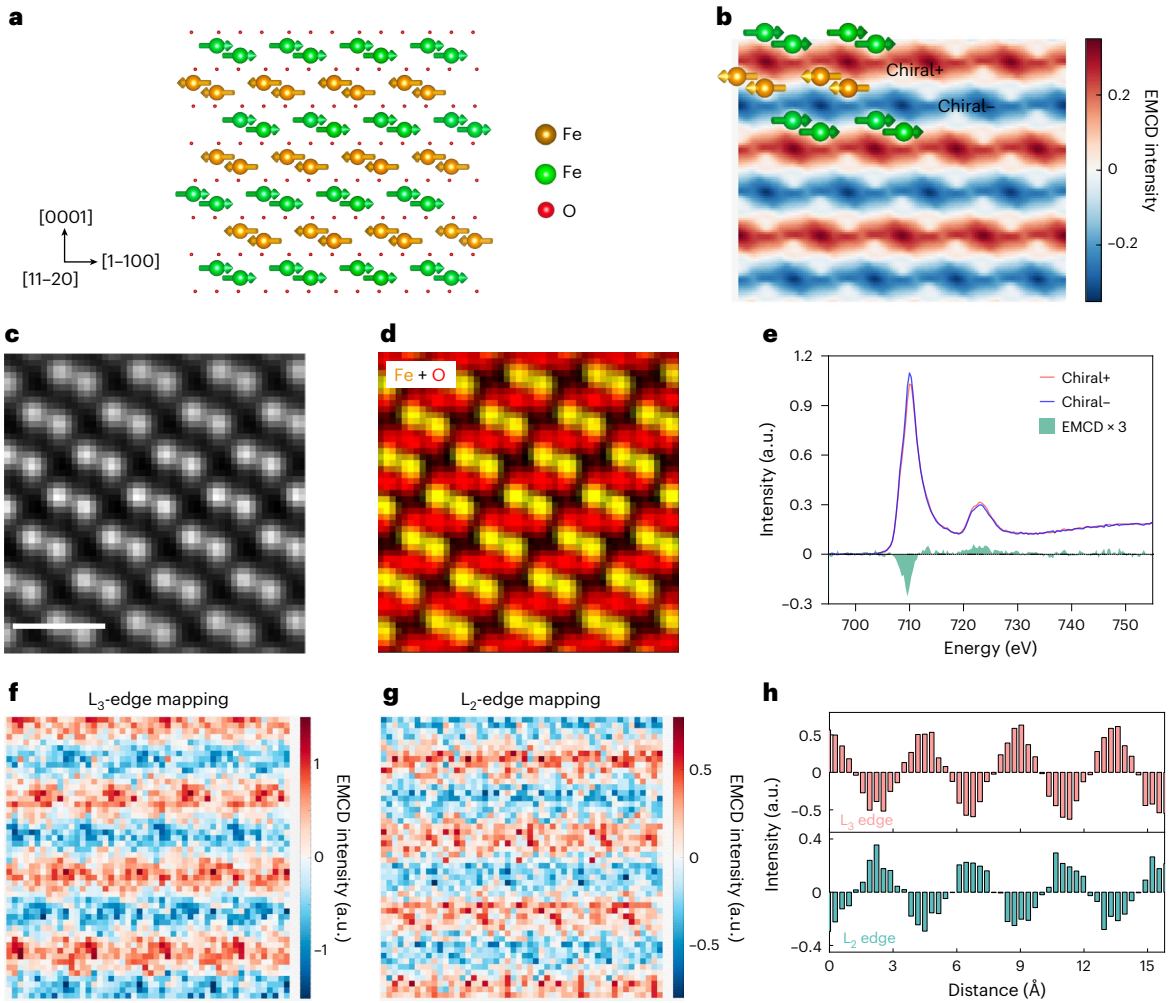

Fig. 3 | Atomic-resolution EMCD signals in α-Fe_2O_3. a, Atomic model of α-Fe_2O_3 projected along the [11$\bar{2}$0] direction, with the spin orientations of Fe atoms aligned along [1$\bar{1}$00] within the *a*–*b* plane. **b**, Simulated real-space EMCD signal distribution for the region shown in **a**. The chiral+ and chiral− regions are indicated. **c**, ADF image obtained after template-matching processing. **d**, Combined elemental maps of Fe and O. **e**, Averaged chiral EELS and the corresponding EMCD signals extracted from the chiral+ and chiral− regions across the entire STEM-EELS datacube. **f**,**g**, EMCD maps generated by integrating the EMCD signals at the L_3 (**f**) and L_2 (**g**) edges, respectively. **h**, Line profiles extracted from the L_3 and L_2 EMCD maps shown in **f** and **g**, respectively, averaged in the horizontal direction. Images in **c**, **d**, **f** and **g** have the same size. Scale bar, 5 Å.

the entire atomic model (Fig. 2a). The electron beam was aligned along the *z* axis and the Fe spins were oriented along the *x* axis at room temperature. The Néel temperature of $DyFeO_3$ is $T_N = 645$ K. The magnetic moment of Dy is quenched at room temperature ($T_N^{Dy} = 4.5$ K)[19] and is, therefore, neglected here. For each scanning point in the supercell, the non-magnetic and magnetic EMCD signals in the diffraction plane were calculated. The simulation was performed for an accelerating voltage of 300 kV, a beam convergence semiangle of 17.8 mrad and a sample thickness of 22.38 nm. Diffraction patterns for each scanning point are provided in Extended Data Fig. 1. The simulated real-space distributions of the EMCD signals are shown in Fig. 2b for Fe (Supplementary Note 2 and Supplementary Fig. 2). The atomic-column-resolved EMCD signals are clearly distinguishable with an alternating pattern, showing a localized distribution between the Fe atomic columns, as indicated by the overlaid atomic model. We define the chiral+ and chiral− positions in Fig. 2b. By subtracting the EELS signals at these two chiral positions, the EMCD signal from the individual atomic columns can be isolated. Since the experimental conditions affect the EMCD signals significantly[18,21], we also calculated the EMCD intensity as a function of the convergence semiangle and sample thickness (Extended Data Fig. 2). We found that the EMCD signal remains stable for sample thicknesses below 40 nm and for convergence semiangles between 10 and 25 mrad, offering feasibility for experiments.

A STEM-EELS datacube was recorded experimentally from a $DyFeO_3$ crystal, with a pixel size of approximately 0.3 Å. Details of the setup and parameters are provided in Methods and Extended Data Fig. 3. To enhance the signal-to-noise ratio, a template-matching method was applied[22,23] (Methods). Elemental maps were calculated by integrating the EELS signals at the Dy $M_{5,4}$, Fe $L_{3,2}$ and O K edges (Fig. 2c). The composite image reveals the atomic-column positions and species. To visualize the EMCD signal, the EELS signals were first summed at all of the chiral+ and chiral− positions (Fig. 2b). The procedure is outlined in Extended Data Fig. 4. The summed chiral+ and chiral− EELS signals, as well as the resulting EMCD signals obtained by calculating their difference, are shown in Fig. 2d. Noticeable contrast of opposite sign is visible at the L_3 and L_2 edges, demonstrating the feasibility of measuring EMCD at the atomic scale for antiferromagnets that have zero net magnetization. The ratio of orbital to spin magnetic moment was calculated by applying the sum rules[7,8] to the EMCD signals shown in Fig. 2d, yielding a value of 0.01 ± 0.01. This negligible value indicates that the orbital magnetic moment is quenched for Fe^{3+} ions occupying the octahedral crystal

https://doi.org/10.1038/s41565-026-02134-z

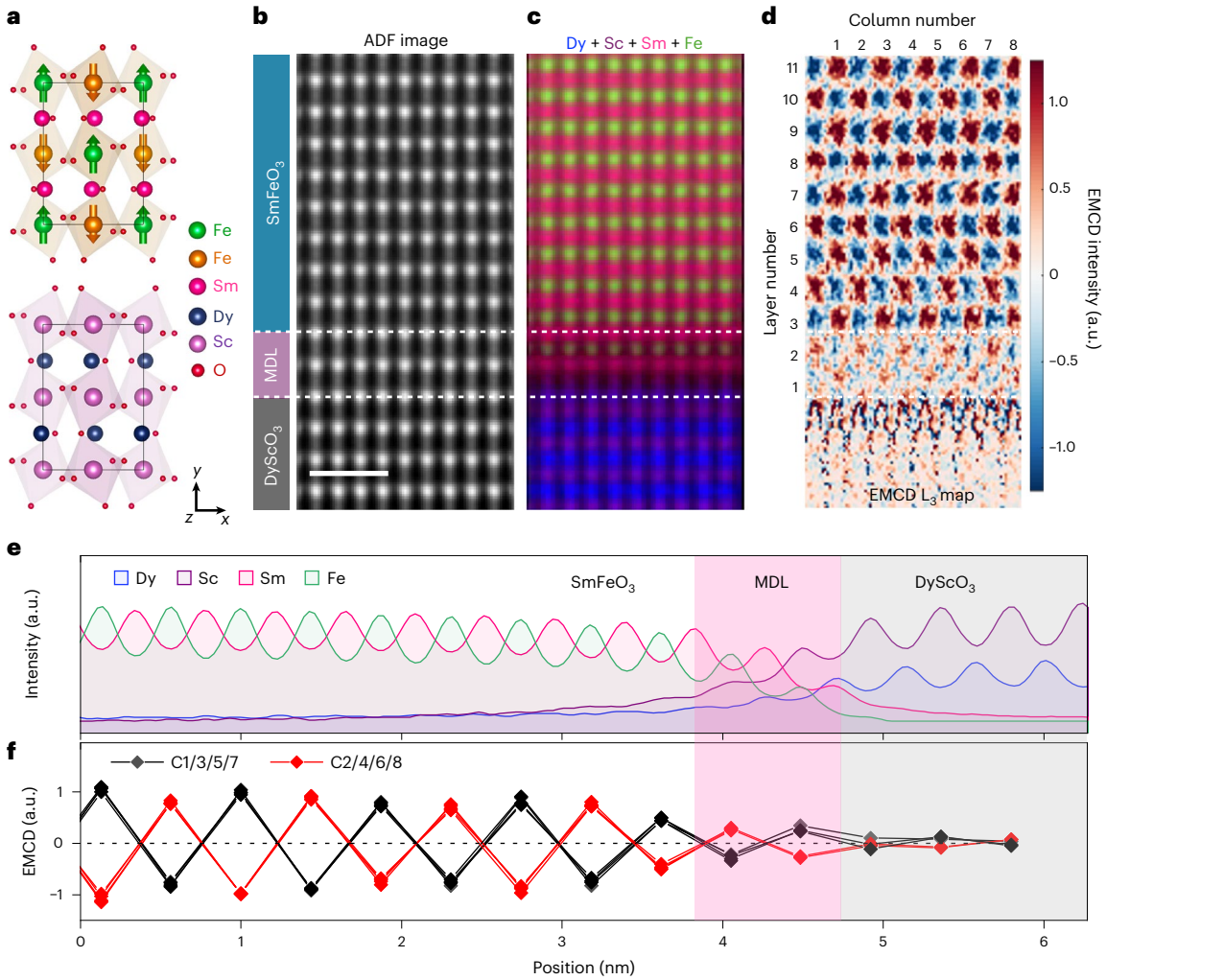

Fig. 4 | MDL at the $DyScO_3$–$SmFeO_3$ interface. a, Atomic models of $DyScO_3$ and $SmFeO_3$ oriented along the *z* axis. The spins in $SmFeO_3$ are aligned along the *y* axis. **b**,**c**, ADF image (**b**) and combined elemental maps (**c**) of Dy (blue), Sc (violet), Sm (pink) and Fe (green) across the interface. **d**, EMCD map generated by integrating the EMCD signals at the L_3 edge. The layer and column numbers are indicated in sequence. **e**,**f**, Extracted profiles of elemental mapping and integrated EMCD signals for individual atomic columns across the interface. The MDL is marked by dashed lines and pink rectangles in **b**–**f**. Scale bar, 1 nm (**b**).

field in $DyFeO_3$ and is consistent with the results of density functional theory calculations[24].

Real-space EMCD maps for the L_3 and L_2 edges are shown in Fig. 2e,f. To generate these maps, chiral+ and chiral− signals were separated from defined regions and averaged to improve the signal-to-noise ratio. Following background removal and post-edge normalization of the chiral EELS data, the EMCD signal was obtained through subtraction, and the EMCD maps were generated by integrating the differential signal at the respective L_3 and L_2 edges. Details of data processing are given in Extended Data Fig. 5. The alternating L_3 and L_2 patterns in the real-space maps are associated with antiferromagnetic ordering and are consistent with the simulations shown in Fig. 2b. Furthermore, the EMCD signals from individual atomic columns were extracted along the horizontal and vertical directions marked in Fig. 2e (Fig. 2g,h). The negative L_3 (L_2) and positive L_2 (L_3) signals are clearly resolved for the Fe atom columns. These features demonstrate successful atomic-column imaging of antiferromagnetic ordering in $DyFeO_3$. The antiferromagnetic ordering was further verified by analysing the atomic-column EMCD signals on the assumption that the spins were oriented along the *y* or *z* directions (Extended Data Figs. 6 and 7, Supplementary Notes 3 and 4, and Supplementary Figs. 3 and 4). The negligible EMCD signals in these measurements confirm that the spins are oriented along the *x* direction.

Imaging antiferromagnetic order in α-Fe_2O_3

To demonstrate its applicability to different antiferromagnetic structures, we applied our technique to haematite (α-Fe_2O_3). α-Fe_2O_3 has a hexagonal crystal structure and exhibits nearly C-type antiferromagnetic ordering, with a Néel temperature of $T_N \approx 950$ K. The Fe^{3+} magnetic moments are aligned parallel within each (0001) basal plane, showing in-plane easy anisotropy in the $< 1\bar{1}00 >$ direction. The magnetic moments are antiparallel between successive (0001) planes, resulting in antiferromagnetic order. In our experiments, a thin Fe_2O_3 sample was oriented along the $[11\bar{2}0]$ zone axis with its spins aligned along $[1\bar{1}00]$ (Fig. 3a). The simulated real-space EMCD distribution reveals that the magnetic signals are localized between adjacent (0001) Fe atomic planes (Fig. 3b). To extract the EMCD signal, we separately integrated the EELS signals in alternating chiral+ and chiral− regions (marked in Fig. 3b) between the Fe atomic planes and calculated their difference. Data were processed using the procedure described for $DyFeO_3$. An ADF image and the corresponding elemental map reveal the atomic structure and elemental distribution (Fig. 3c,d). Summed EELS signals from the chiral+ and chiral− regions yield distinct EMCD signals (Fig. 3e), confirming the feasibility of atomic-column EMCD for C-type antiferromagnets. The integrated EMCD signals at the L_3 and L_2 edges reveal the expected antiferromagnetic contrast (Fig. 3f,g), consistent with the simulated results (Fig. 3b). A line profile of the EMCD

intensity across the (0001) planes (Fig. 3h), shows alternating signal polarity, consistent with an antiferromagnetic coupling.

MDL at the $DyScO_3$–$SmFeO_3$ interface

MDLs—regions in which magnetic order is significantly suppressed—often form at interfaces between magnetic materials and adjacent substrates or capping layers, critically influencing spintronic device performance and fundamental magnetic interactions. However, directly probing these interfacial MDLs at the atomic scale remains challenging due to the limited spatial resolution of conventional magnetic characterization techniques. Here we apply atomic-column-resolved EMCD to map the magnetism across the interface between $DyScO_3$ and the antiferromagnetic $SmFeO_3$ (Fig. 4a, Methods and Extended Data Fig. 8 show the film growth and structural characterization). The small lattice mismatch between $DyScO_3$ and $SmFeO_3$ leads to a fully coherent interface (Fig. 4b).

$SmFeO_3$ has an orthorhombic crystal structure with a Néel temperature of around 640 K. The Fe^{3+} ions exhibit G-type antiferromagnetic ordering with spins oriented along the *y* axis[25], whereas the Sm^{3+} ions are non-magnetic at room temperature (Fig. 4a). This contrasts with the *x*-axis spin orientation in $DyFeO_3$ (Fig. 2a). In this case, the EMCD signals are distributed between adjacent Fe columns, as demonstrated in simulations (Extended Data Fig. 6). Elemental and EMCD signals mappings are shown in Fig. 4c,d, and the corresponding line profiles across the interface are presented in Fig. 4e,f. The localized EMCD signals between adjacent Fe columns in Fig. 4d confirm that the spins are oriented along the *y* axis in $SmFeO_3$. The column-by-column EMCD spectra are shown in Supplementary Note 5 and Supplementary Fig. 5. These results unambiguously reveal a magnetically suppressed interfacial region with a thickness of one unit cell as the antiferromagnetic coupling is preserved (Fig. 4d). The fully strained nature of the thin film allows us to conclusively attribute this magnetic suppression to interfacial interdiffusion, as evidenced by the chemically intermixed region (Fig. 4e, pink areas) with a composition describable as $(Sm_{1-x}Dy_x)(Fe_{1-y}Sc_y)O_3$. Although previous studies proposed various mechanisms for MDL formation, including interfacial diffusion, strain effects and emergent magnetic coupling[26], our direct measurements provide definitive evidence that chemical interdiffusion plays a dominant role in this system.

The measurement of antiferromagnetic ordering across the interface benefits from atomic-column lateral resolution. With a minimum Fe–Fe atomic-column spacing of approximately 2.65 Å in the present system, our method is also well suited for probing magnetic variations at other defects, such as twin boundaries, stacking faults, and, in principle, dislocations or point defects, provided that the atomic arrangement is well defined and that the sample can tolerate the required electron dose (Supplementary Note 6 and Supplementary Fig. 6). By comparison, atomic-column-resolved DPC imaging typically relies on spatial averaging over several neighbouring unit cells to reconstruct local magnetic fields[5], which restricts its applicability to nearly perfect crystalline regions. Similarly, although electron holography[4] and conventional EMCD[10–12] can achieve atomic-plane resolution, they lack atomic-column lateral resolution and are intrinsically insensitive to G-type antiferromagnetic order due to the zero net magnetization per atomic plane.

Conclusions

We establish an atomic-column-resolved EMCD method for the element-specific mapping of magnetic order in antiferromagnets at the atomic scale. The combined zone-axis diffraction geometry and on-axis experimental setup make it broadly accessible in a standard aberration-corrected STEM with EELS. This capability is demonstrated not only by resolving G-type and C-type antiferromagnetic orders in $DyFeO_3$ and α-Fe_2O_3 crystals but also by probing defective regions through mapping an MDL at the buried $DyScO_3$–$SmFeO_3$ interface.

This technique can be used for studying antiferromagnetism and interfacial magnetism, and is readily extendable to emerging phenomena such as altermagnets[27] and topological magnetism[28]. It also offers the potential to link magnetism with atomic and electronic structure, particularly at domain walls and interfaces that exhibit exchange bias or emergent magnetism. In the future, the use of a magnetic-field-free environment in the TEM[4,5,29] can be used to preserve intrinsic magnetic configurations, offering advantages for performing atomic-resolution magnetic studies of ferromagnets and other materials that may be affected by external magnetic fields.

Online content

Any methods, additional references, Nature Portfolio reporting summaries, source data, extended data, supplementary information, acknowledgements, peer review information; details of author contributions and competing interests; and statements of data and code availability are available at https://doi.org/10.1038/s41565-026-02134-z.

References

1. van der Laan, G. et al. Experimental proof of magnetic X-ray dichroism. *Phys. Rev. B* **34**, 6529–6531 (1986).
2. van der Laan, G. & Figueroa, A. I. X-ray magnetic circular dichroism—a versatile tool to study magnetism. *Coord. Chem. Rev.* **277–278**, 95–129 (2014).
3. Cui, J., Sha, H., Yang, W. & Yu, R. Antiferromagnetic imaging via ptychographic phase retrieval. *Sci. Bull.* **69**, 466–472 (2024).
4. Tanigaki, T. et al. Electron holography observation of individual ferrimagnetic lattice planes. *Nature* **631**, 521–525 (2024).
5. Kohno, Y., Seki, T., Findlay, S. D., Ikuhara, Y. & Shibata, N. Real-space visualization of intrinsic magnetic fields of an antiferromagnet. *Nature* **602**, 234–239 (2022).
6. Schattschneider, P. et al. Detection of magnetic circular dichroism using a transmission electron microscope. *Nature* **441**, 486–488 (2006).
7. Rusz, J., Eriksson, O., Novák, P. & Oppeneer, P. M. Sum rules for electron energy loss near edge spectra. *Phys. Rev. B* **76**, 060408 (2007).
8. Calmels, L. et al. Experimental application of sum rules for electron energy loss magnetic chiral dichroism. *Phys. Rev. B* **76**, 060409 (2007).
9. Ali, H. et al. Noise-dependent bias in quantitative STEM-EMCD experiments revealed by bootstrapping. *Ultramicroscopy* **257**, 113891 (2024).
10. Rusz, J. et al. Magnetic measurements with atomic-plane resolution. *Nat. Commun.* **7**, 12672 (2016).
11. Wang, Z. et al. Atomic scale imaging of magnetic circular dichroism by achromatic electron microscopy. *Nat. Mater.* **17**, 221–225 (2018).
12. Ali, H. et al. Visualizing subatomic orbital and spin moments using a scanning transmission electron microscope. *Nat. Mater.* **24**, 1215–1220 (2025).
13. Kimoto, K. et al. Element-selective imaging of atomic columns in a crystal using STEM and EELS. *Nature* **450**, 702–704 (2007).
14. Muller, D. A. et al. Atomic-scale chemical imaging of composition and bonding by aberration-corrected microscopy. *Science* **319**, 1073–1076 (2008).
15. Idrobo, J. C. et al. Detecting magnetic ordering with atomic size electron probes. *Adv. Struct. Chem. Imaging* **2**, 5 (2016).
16. Rusz, J., Rubino, S. & Schattschneider, P. First-principles theory of chiral dichroism in electron microscopy applied to 3*d* ferromagnets. *Phys. Rev. B* **75**, 214425 (2007).
17. Calmels, L. & Rusz, J. Momentum-resolved EELS and EMCD spectra from the atomic multiplet theory: application to magnetite. *Ultramicroscopy* **110**, 1042–1045 (2010).

18. Song, D. & Dunin-Borkowski, R. E. Three-dimensional measurement of magnetic moment vectors using electron magnetic chiral dichroism at atomic scale. *Phys. Rev. Lett.* **127**, 087202 (2021).
19. Ritter, C. et al. The magnetic structure of $DyFeO_3$ revisited: Fe spin reorientation and Dy incommensurate magnetic order. *J. Phys. Condens. Matter* **34**, 265801 (2022).
20. Song, D. et al. An in-plane magnetic chiral dichroism approach for measurement of intrinsic magnetic signals using transmitted electrons. *Nat. Commun.* **8**, 15348 (2017).
21. Rusz, J. et al. Localization of magnetic circular dichroic spectra in transmission electron microscopy experiments with atomic plane resolution. *Phys. Rev. B* **95**, 174412 (2017).
22. Jones, L. et al. Managing dose-, damage- and data-rates in multi-frame spectrum-imaging. *Microscopy* **67**, i98–i113 (2018).
23. Haruta, M. et al. Atomic-resolution two-dimensional mapping of holes in the cuprate superconductor $La_{2-x}Sr_xCuO_{4\pm\delta}$. *Phys. Rev. B* **97**, 205139 (2018).
24. Cui, R. et al. Role of Dy 4*f* electrons on magnetic coupling and reorientation in $DyFeO_3$. *J. Phys. Condens. Matter* **36**, 335501 (2024).
25. Kuo, C.-Y. et al. $k=0$ magnetic structure and absence of ferroelectricity in $SmFeO_3$. *Phys. Rev. Lett.* **113**, 217203 (2014).
26. Luo, W. et al. Magnetic 'dead' layer at a complex oxide interface. *Phys. Rev. Lett.* **101**, 247204 (2008).
27. Šmejkal, L., Sinova, J. & Jungwirth, T. Emerging research landscape of altermagnetism. *Phys. Rev. X* **12**, 040501 (2022).
28. Bernevig, B. A., Felser, C. & Beidenkopf, H. Progress and prospects in magnetic topological materials. *Nature* **603**, 41–51 (2022).
29. Shibata, N. et al. Atomic resolution electron microscopy in a magnetic field free environment. *Nat. Commun.* **10**, 2308 (2019).

[1]State Key Laboratory of Opto-Electronic Information Acquisition and Protection Technology, Institutes of Physical Science and Information Technology, Anhui University, Hefei, China. [2]Ernst Ruska-Centre for Microscopy and Spectroscopy with Electrons, Forschungszentrum Jülich, Jülich, Germany. [3]Spin-X Institute, Center for Electron Microscopy, School of Physics and Optoelectronics, State Key Laboratory of Luminescent Materials and Devices, Guangdong-Hong Kong-Macao Joint Laboratory of Optoelectronic and Magnetic Functional Materials, South China University of Technology, Guangzhou, China. [4]Anhui Key Laboratory of Condensed Matter Physics at Extreme Conditions, High Magnetic Field Laboratory, HFIPS, Anhui, Chinese Academy of Sciences, Hefei, China. [5]School of Physics and Mechanics, Wuhan University of Technology, Wuhan, China. [6]School of Physics and Optoelectronic Engineering, Anhui University, Hefei, China. ✉e-mail: dsong@ahu.edu.cn; duhf@hmfl.ac.cn

Methods

Sample preparation

A $DyFeO_3$ single crystal was grown using a floating zone method[30]. The [0001]-oriented α-Fe_2O_3 single crystal was purchased from MTI Corporation. Epitaxial thin film of $SmFeO_3$ were grown on a $DyScO_3$(001) substrate using the pulsed laser deposition technique. The substrate temperature and oxygen pressure during deposition were set to 850 °C and 0.05 mbar, respectively. Pulsed laser deposition was performed with a KrF excimer ultraviolet laser (λ = 248 nm), using an energy density of 1.5 J cm^{-2} and a repetition rate of 2 Hz. After deposition, the films were cooled to room temperature at a rate of 10 °C min^{-1} under an oxygen partial pressure of approximately 0.5 bar. For the TEM and EMCD experiments, the samples were initially thinned to electron transparency by using a focused-ion-beam system (Helios NanoLab 600i, FEI) equipped with an Omniprobe 200+ micromanipulator at 30 kV. The amorphous layer on the sample surface was removed at 2 kV. The focused-ion-beam lamellae were further processed with Ar ions at 3 kV on a Bal-Tec RES 101 ion-beam milling system and at 900 V and 500 V on a Fischione NanoMill 1040 system, to thin them further and to eliminate surface damage.

EMCD simulations

EMCD simulations were performed using MATS (v. 2) software, which uses a combined multislice and Bloch-wave method[31,32]. Chiral EELS signals in the diffraction plane, which are evaluated based on a double-differential scattering cross-section for momentum-resolved inelastic electron scattering, can be expressed as a linear superposition of non-magnetic and magnetic EMCD contributions within the dipole approximation:

$$\frac{\partial^2\sigma}{\partial E\partial\Omega} \propto \mathrm{A} \times N(E) + B \times M(E),$$

where $N(E)$ and $M(E)$ are the non-magnetic and magnetic EMCD signals, respectively. For non-magnetic materials, $M(E)$ is zero. The coefficients A and B represent the intensities of the non-magnetic and magnetic EMCD signals, respectively. They are determined from the product of Bloch coefficients and momentum transfers[32] and are influenced by experimental parameters, including the crystal structure, sample thickness and imaging conditions. The relative intensity of the EMCD signal is defined as the ratio B/A. Magnetic signals from the three Cartesian directions can be separately calculated by modifying the momentum transfer terms.

In the simulations, the orthogonal supercells of $DyFeO_3$, α-Fe_2O_3 and $SmFeO_3$ were constructed and oriented along the desired directions, with the electron beam parallel to the z axis. All aberrations were set to zero. The accelerating voltage, beam position, convergence semiangle and sample thickness were adjusted as required. An energy loss of 710 eV, corresponding to the Fe L_3 edge, was used to calculate the energy-selected diffraction patterns. At a fixed electron-beam position, the distributions of the non-magnetic and magnetic EMCD signals were computed for each pixel in the diffraction plane. The diffraction pattern range was set to ±40 mrad in the q_x and q_y directions with a step size of 2.5 mrad (Figs. 1c–e, 2b and 3b, and Extended Data Fig. 1). Note that in antiferromagnetic $DyFeO_3$, the Fe atoms form two magnetic sublattices with opposite spin orientations. In our simulations, we explicitly separate the non-magnetic and magnetic contributions from each sublattice. The final EMCD signal is obtained by taking the difference between their respective magnetic contributions. The details are presented in Supplementary Note 2 and Supplementary Fig. 2.

STEM experiments

The atomic structure of the crystals was imaged using high-angle annular dark-field (HAADF) STEM and integrated DPC STEM (Extended Data Fig. 8). Experiments were conducted on a Thermo Fisher Scientific Titan Themis Z microscope operated at 300 kV. This microscope is equipped with a probe corrector, a four-segment DF4 detector and a Gatan GIF Continuum K3 dual-EELS system. The convergence semiangle for STEM imaging was set to 25 mrad, with collection semiangles of 50–200 mrad for HAADF imaging and 8–42 mrad for integrated DPC imaging. The beam current was 30 pA. Integrated DPC images were reconstructed from four-segment images, making use of a high-pass filter to eliminate low-frequency information. Data acquisition and processing were performed using commercial Velox software (version 3.18). The sample thickness was measured using position-averaged convergent beam electron diffraction (PACBED) (Extended Data Fig. 3). The convergence semiangle for PACBED was approximately 6.75 mrad and PACBED patterns were recorded using the K3 camera. PACBED simulations were performed using the Dr. Probe software[33] for the same parameters as those used in the experiments.

Atomic-column EMCD experiments

Atomic-column EMCD experiments used the same experimental setup as conventional atomic-column STEM-EELS, using an on-axis EELS entrance aperture and requiring no additional facilities or modifications. The convergence semiangle was optimized to be ~17.8 mrad. The collection semiangle was calibrated to be ~40 mrad. EELS signals were recorded using a K3 camera installed on the post-column Gatan imaging filter. The beam current was set to 50–80 pA with a pixel dwell time of 2–3 ms, as a result of its resistance to irradiation damage. The pixel size was 0.325 Å and the EELS energy dispersion was set to 0.35 eV per channel.

The primary difference between this setup and that used for conventional EMCD results from the localization of the magnetic signals around the directly transmitted electron beam, which allows for the use of an on-axis aperture, and, in turn, offers a significantly improved signal-to-noise ratio compared with previous off-axis acquisition methods (Supplementary Note 1 and Supplementary Fig. 1). This concept relies on the magnetization being oriented perpendicular to the electron-beam direction, facilitating the redistribution of signals in the diffraction plane[11,12]. Moreover, the zone-axis EMCD geometry is robust against beam misorientation, maintaining stable signal strength and spatial distribution for tilt variations up to 5 mrad in $DyFeO_3$ (Supplementary Note 7 and Supplementary Fig. 7). This tolerance is significantly broader than that of a conventional three-beam configuration[11,12], which typically requires sub-milliradian alignment to preserve signal integrity.

Extraction of atomic-column-by-atomic-column EMCD signals

Atomic-column EMCD signals were extracted from the experimental STEM-EELS datacubes, in which the x and y directions correspond to the scanning regions in real space and the z axis represents energy loss. The STEM-EELS experiments generate three data files: an atomic-column-resolved ADF image (size, $m \times n$), a corresponding low-loss EELS datacube (size, $m \times n \times p$) and a high-loss EELS datacube (size, $m \times n \times p$). Energy calibration is first performed on the high-loss datacube by aligning the peak of the low-loss datacube to zero using the DigitalMicrograph software (version 3.53). Subsequently, data processing involves (1) summing the EELS signals at the chiral+ and chiral− positions, as defined in Figs. 2b and 3b, to visualize the averaged EMCD signals (Figs. 2d and 3e) and (2) mapping the EMCD signals in real space with atomic-column resolution (Figs. 2e,f, 3f,g and 4d).

In the first case, the procedure is outlined in the form of a flowchart (Extended Data Fig. 4). The positions of the Dy and Fe atomic columns are identified and fitted based on the ADF image. For each of the defined chiral positions (chiral+ and chiral−), the EELS signals are extracted and summed. Post-processing steps, including background removal and post-edge normalization, are applied to the two chiral EELS signals. The EMCD signal is obtained by calculating the difference between the chiral+ and chiral− signals (Fig. 2d).

In the second case, the procedure is outlined in Extended Data Fig. 5. As in the first case, the Dy and Fe atomic-column positions are identified and fitted from the ADF image. Taking the position of the Dy atoms as the centre, a region of interest with a size of 50 × 50 pixels is extracted. The regions of interest are divided into two groups: the ADF stack for chiral+ ($50 \times 50 \times N^{+}$) and the ADF stack for chiral− ($50 \times 50 \times N^{-}$). There is a half-unit-cell offset between the two chiral datasets. Note that this offset leads to the mixing of inequivalent atomic sites in $DyFeO_3$, particularly the oxygen sublattices, when subtracting the two stacks to obtain the final EMCD maps. This issue arises in $DyFeO_3$ but does not occur in all systems, such as in α-Fe_2O_3 (Fig. 3). However, since the EMCD technique is element specific, misalignment of the oxygen sublattice would not significantly influence the EMCD maps at the Fe L edges (Supplementary Note 8 and Supplementary Fig. 8 discuss the simulation test and discussion), particularly after the background removal and post-edge normalization of the EELS signals at each pixel (Extended Data Fig. 5, in which the spectrum image of the Fe sublattice after background removal and post-edge normalization is nearly identical between the two datasets). Additionally, in STEM-EELS experiments with a long acquisition time, instrumental instabilities and sample drift can introduce distortions in both ADF and the EELS stacks, leading to slight deviations from perfectly conjugate probe positions.

To address the potential misalignments arising from both lattice distortion and sample drift, we applied non-rigid image registration between the chiral+ and chiral− datasets. This approach ensures accurate alignment before subtraction, thereby minimizing residual lattice offsets and preventing potentional artificial contrast. Then, the two ADF stacks are summed to generate two ADF images. The same procedure is applied to the high-loss datacube, yielding two EELS datacubes (chiral+ and chiral−) with improved signal-to-noise ratio. Finally, post-processing steps, including background removal and post-edge normalization, are applied to the two datacubes. The EMCD datacube is obtained by calculating the difference between the chiral+ and chiral− datacubes. The magnetic ordering maps shown in Fig. 2e,f were obtained by integrating the EMCD signals at the L_3 and L_2 edges. For the $DyScO_3$–$SmFeO_3$ interface, signal averaging was performed in a similar way, with data acquired by conducting multiple STEM-EELS measurements across the interface.

Additionally, we processed our data using the alternative approach outlined below, without applying a half-unit-cell shift described in Extended Data Fig. 5. (1) We defined the mean Fe L-edge spectrum (Fe_mean) as the average of the two chiral spectra shown in Extended Data Fig. 4. (2) We compared this Fe_mean spectrum with the Fe L-edge spectra extracted from the Dy-site regions in the spectrum images. (3) We calculated the difference between the Dy-site region of interest spectra and the Fe_mean spectrum at both L_3 and L_2 edges to generate the EMCD maps. On the basis of this procedure, we calculated the EMCD maps at the L_3 and L_2 edges (Extended Data Fig. 9) for $DyFeO_3$, and Supplementary Note 9 and Supplementary Fig. 9 discuss these data for the $DyScO_3$–$SmFeO_3$ interface. The results also clearly reveal the antiferromagnetic ordering, providing complementary validation of our conclusions.

Data availability

Raw experimental data and key processed results for this study are available via Zenodo at https://doi.org/10.5281/zenodo.18238440 (ref. 34). All other data supporting the findings of this study are included in the article and its Supplementary Information. Additional information related to this work can be obtained from the corresponding authors upon reasonable request.

References

30. Ke, Y.-J., Zhang, X.-Q., Ge, H., Ma, Y. & Cheng, Z.-H. Low field induced giant anisotropic magnetocaloric effect in $DyFeO_3$ single crystal. *Chinese Phys. B* **24**, 037501 (2015).
31. Rusz, J., Bhowmick, S., Eriksson, M. & Karlsson, N. Scattering of electron vortex beams on a magnetic crystal: towards atomic-resolution magnetic measurements. *Phys. Rev. B* **89**, 134428 (2014).
32. Rusz, J. Modified automatic term selection v2: a faster algorithm to calculate inelastic scattering cross-sections. *Ultramicroscopy* **177**, 20–25 (2017).
33. Barthel, J. Dr. Probe: a software for high-resolution STEM image simulation. *Ultramicroscopy* **193**, 1–11 (2018).
34. Song, D. et al. Source data for atomic-column EMCD technique. *Zenodo* https://doi.org/10.5281/zenodo.18238440 (2026).

Acknowledgements

We are grateful for financial support from the National Key R&D Program of China (number 2022YFA1403603) (D.S. and H.D.), the National Natural Science Foundation of China (numbers 52173215 (D.S.), 52473226 (D.S.), 12241406 (H.D.) and 52325105 (H.D.)), the National Natural Science Fund for Excellent Young Scientists Fund Program (Overseas, 2021) (D.S.), the CAS Project for Young Scientists in Basic Research (YSBR-084) (H.D.), the Strategic Priority Research Program of the Chinese Academy of Sciences (XDB33030100) (H.D.) and the Chinese Academy of Sciences under contract number JZHKYPT-2021-08 (H.D.). F.Z. acknowledges financial support from the Fundamental Research Funds for the Central Universities and the National Natural Science Fund for Excellent Young Scientists Fund Program (Overseas). R.E.D.-B. is grateful for financial support from the European Research Council under the European Union's Horizon 2020 research and innovation programme (grant number 856538, project '3D MAGiC') and the Deutsche Forschungsgemeinschaft (project ID 405553726; TRR 270). This work made use of the resources of the Center for Electron Microscopy at Anhui University and the Ernst Ruska Centre for Microscopy and Spectroscopy with Electrons at Forschungszentrum Jülich. D.S. thanks J. Rusz for providing MATS (v. 2) software and helpful discussion.

Author contributions

D.S., H.D. and R.E.D.-B. supervised the study. D.S. conceived the idea and initiated the study. D.S. conducted the EMCD simulations and experiments and analysed the data. H.D. prepared the TEM sample. L.H. prepared the $SmFeO_3$ thin films. L.J. performed the NanoMill experiments. Y.K. synthesized the $DyFeO_3$ crystal. B.G. and M.T. provided support for the facilities. D.S. and F.Z. wrote the paper with input from H.D., Y.L. and R.E.D.-B. All authors discussed the results and contributed to the paper.

Competing interests

The authors declare no competing interests.

Additional information

Extended data is available for this paper at https://doi.org/10.1038/s41565-026-02134-z.

Supplementary information The online version contains supplementary material available at https://doi.org/10.1038/s41565-026-02134-z.

Correspondence and requests for materials should be addressed to Dongsheng Song or Haifeng Du.

Peer review information *Nature Nanotechnology* thanks Juan Idrobo and the other, anonymous, reviewer(s) for their contribution to the peer review of this work.

https://doi.org/10.1038/s41565-026-02134-z

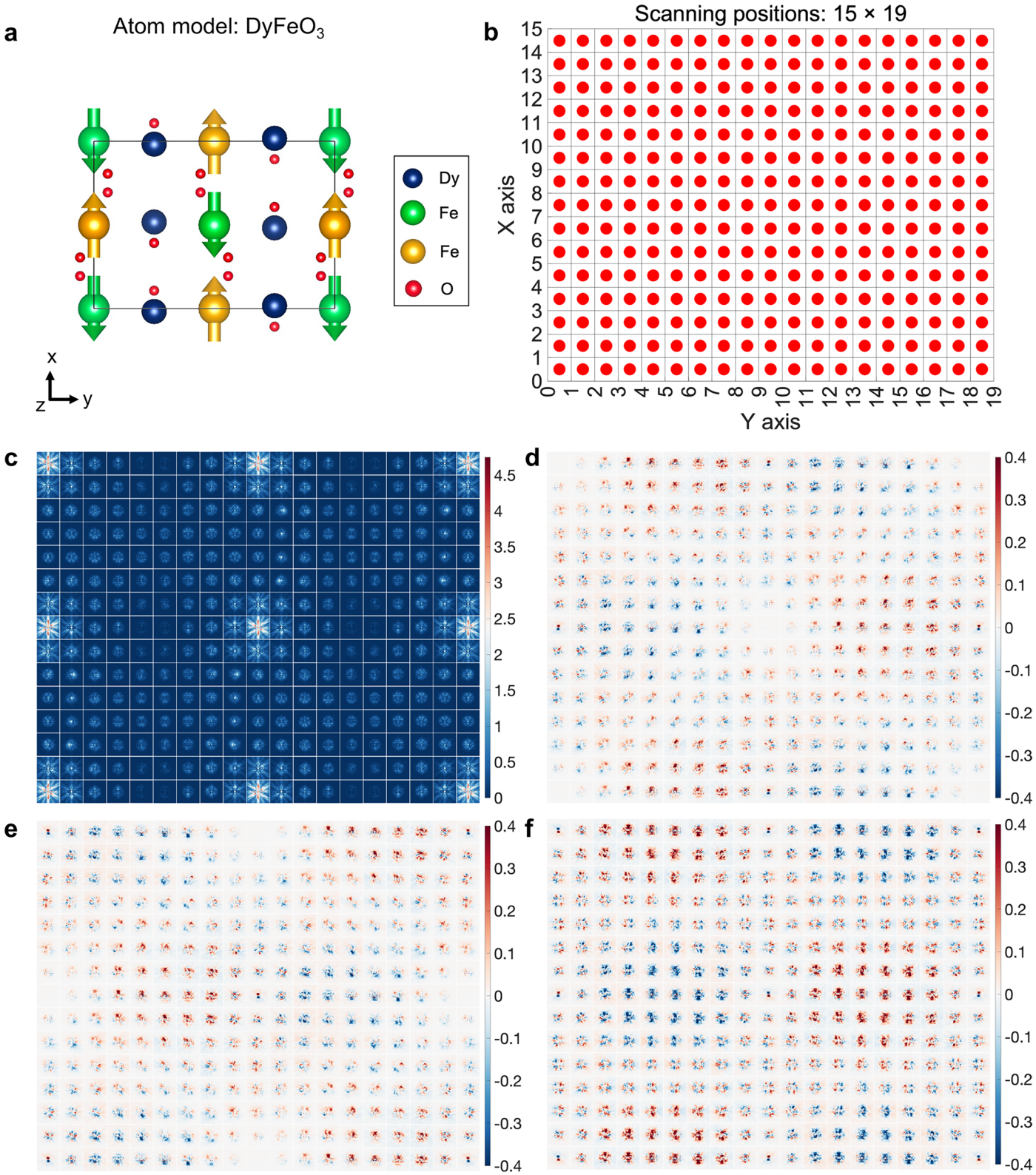

Extended Data Fig. 1 | Simulated distributions of Fe EMCD signals across a unit cell of $DyFeO_3$. **a**, Atomic model of $DyFeO_3$ projected along the *z* direction, with the Fe spins oriented along the *x*-axis. **b**, Mesh grid representation of the unit cell, consisting of a 15 × 19 grid. The grid points mark the scanning probe positions in real space. **c**, Simulated nonmagnetic signals in the diffraction plane at each probe position. Each individual image in **c** shows the signal distribution in the diffraction plane, spanning $q_x = \pm 40$ mrad and $q_y = \pm 40$ mrad. **d**,**e**, Simulated EMCD signals in the diffraction plane at each probe position for Fe sublattices with spin orientations along the +*x* and -*x* directions, respectively. **f**, Total EMCD signals at each position, obtained by computing the difference between **d** and **e**. By integrating the signals in the diffraction plane using an *on-axis* EELS entrance aperture (collection semi-angle 40 mrad) in **d**-**f**, a real-space mapping of the EMCD signals across the unit cell is obtained, as shown in Fig. 2b.

https://doi.org/10.1038/s41565-026-02134-z

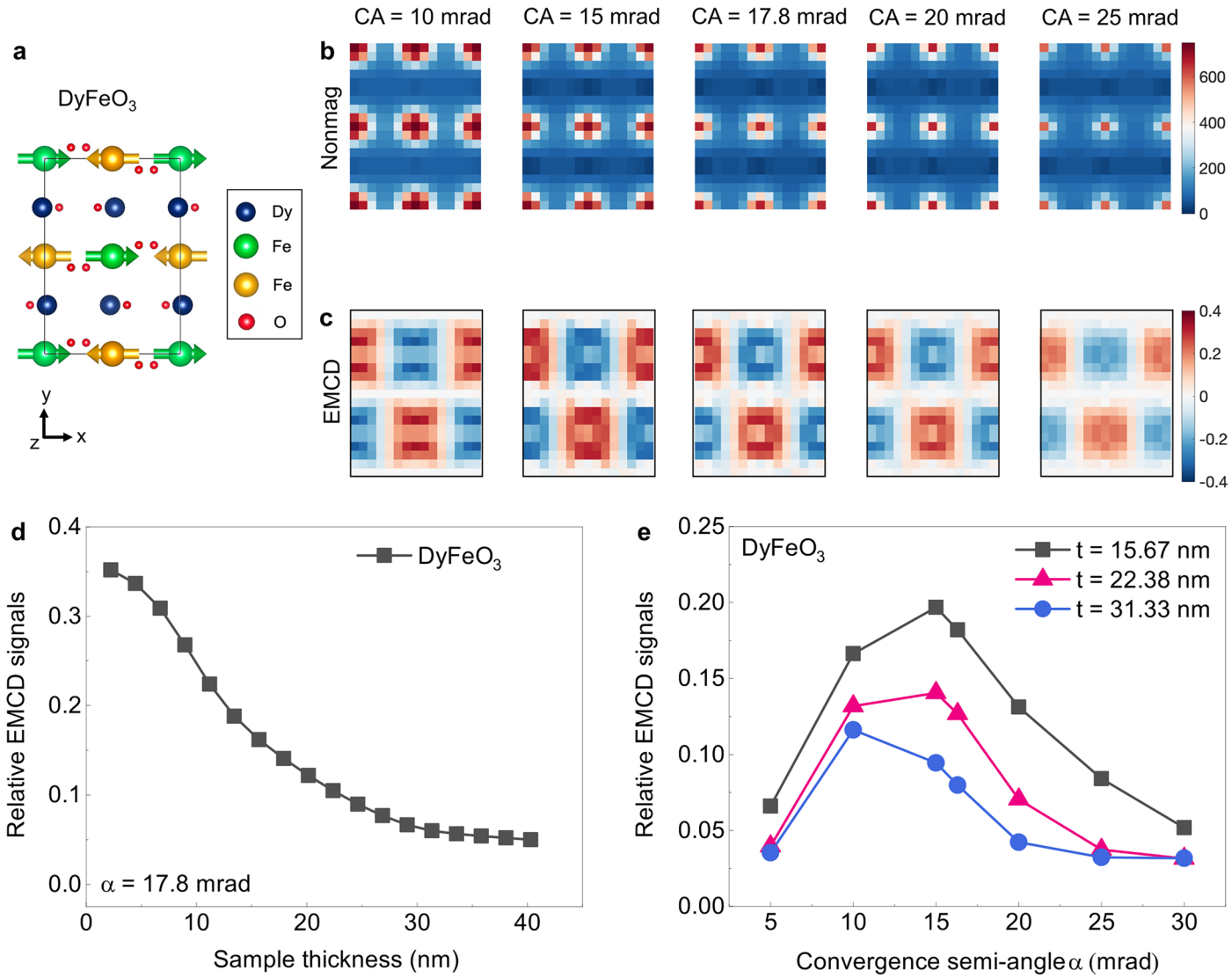

Extended Data Fig. 2 | Effect of convergence semi-angle and sample thickness on EMCD signal intensity. a, Atomic model of $DyFeO_3$ projected along the *z* direction, with the Fe spins oriented along the *x* direction. **b**,**c**, Distributions of nonmagnetic and EMCD signals, respectively, across the unit cell for varying convergence semi-angle (CA). The sample thickness is 22.38 nm. **d**, Relative intensities of EMCD signals plotted as a function of sample thickness for $DyFeO_3$. The CA is 17.8 mrad. **e**, Relative intensities of EMCD signals plotted as a function of CA for three different sample thicknesses of $DyFeO_3$. In the experiments, the sample thickness is approximately 13 nm for $DyFeO_3$.

https://doi.org/10.1038/s41565-026-02134-z

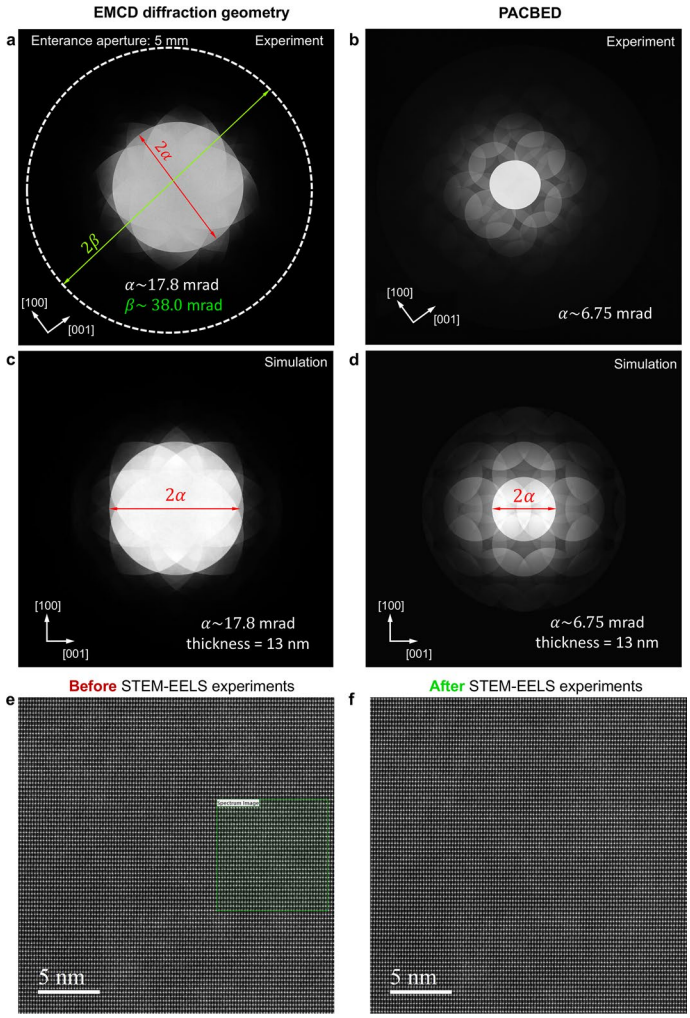

Extended Data Fig. 3 | Experimental diffraction geometry and setup for the atomic-column EMCD technique. a, Experimental diffraction pattern recorded from $DyFeO_3$ oriented along the *z*-axis. The white dashed circle marks the EELS 5 mm entrance aperture, which has a collection semi-angle β of approximately 38 mrad in the current experiments. The convergence semi-angle α is 17.8 mrad. **b**, Experimental PACBED pattern for $DyFeO_3$ oriented along the *z*-axis. The convergence semi-angle is 6.75 mrad. **c**, Simulated diffraction pattern for the same conditions as in **a**. **d**, Simulated PACBED pattern for the same conditions as in **a**. The sample thickness is determined to be 13 nm using PACBED. **e,f**, ADF images recorded before and after STEM-EELS acquisition. The green box in **e** marks the regions used for STEM-EELS acquisition. No significant changes in the sample were observed after the experiments.

https://doi.org/10.1038/s41565-026-02134-z

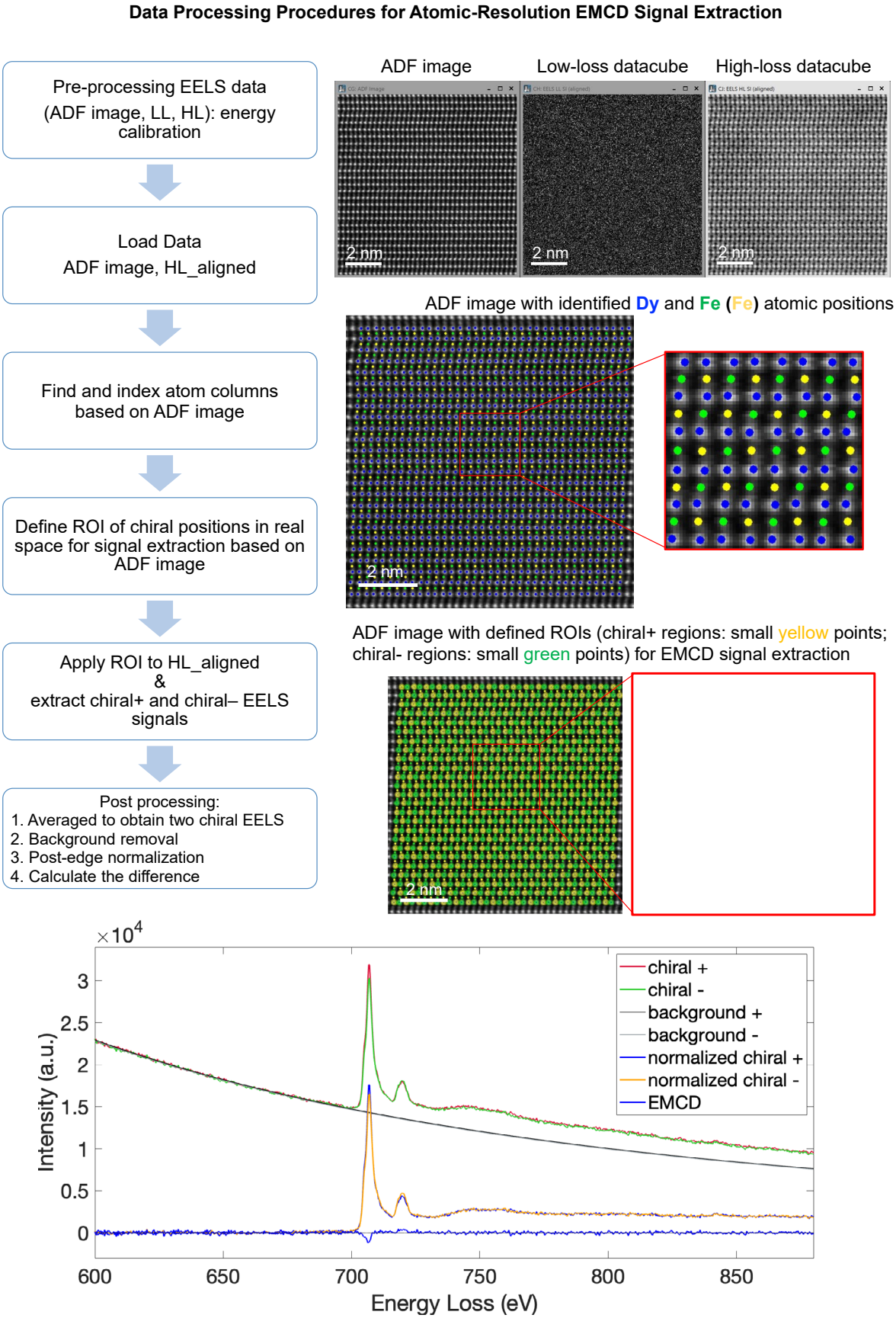

Extended Data Fig. 4 | See next page for caption.

https://doi.org/10.1038/s41565-026-02134-z

Extended Data Fig. 4 | Data processing procedure for atomic-column-by-atomic-column EMCD signal extraction. (1) The STEM-EELS experiments generate the following data files: ADF image; low-loss EELS (LL); high-loss EELS (HL). An energy calibration is performed based on the LL data using Digital Micrograph software. (2) The ADF image is used to identify and fit the positions of the Dy and Fe atomic columns. The Fe columns are indexed using different colored dots to distinguish their spin orientations. (3) In order to extract EMCD signals from the chiral+ and chiral- positions, regions of interest (ROIs) - represented by yellow and green small dots - are defined and localized at the Dy atom positions based on the EMCD simulations shown in Fig. 2b. (4) All of the EELS signals at the chiral+ and chiral- positions are summed. (5) Post-processing, including background removal and post-edge normalization, is applied to the two chiral EELS signals. The EMCD signal is the difference between these two signals.

https://doi.org/10.1038/s41565-026-02134-z

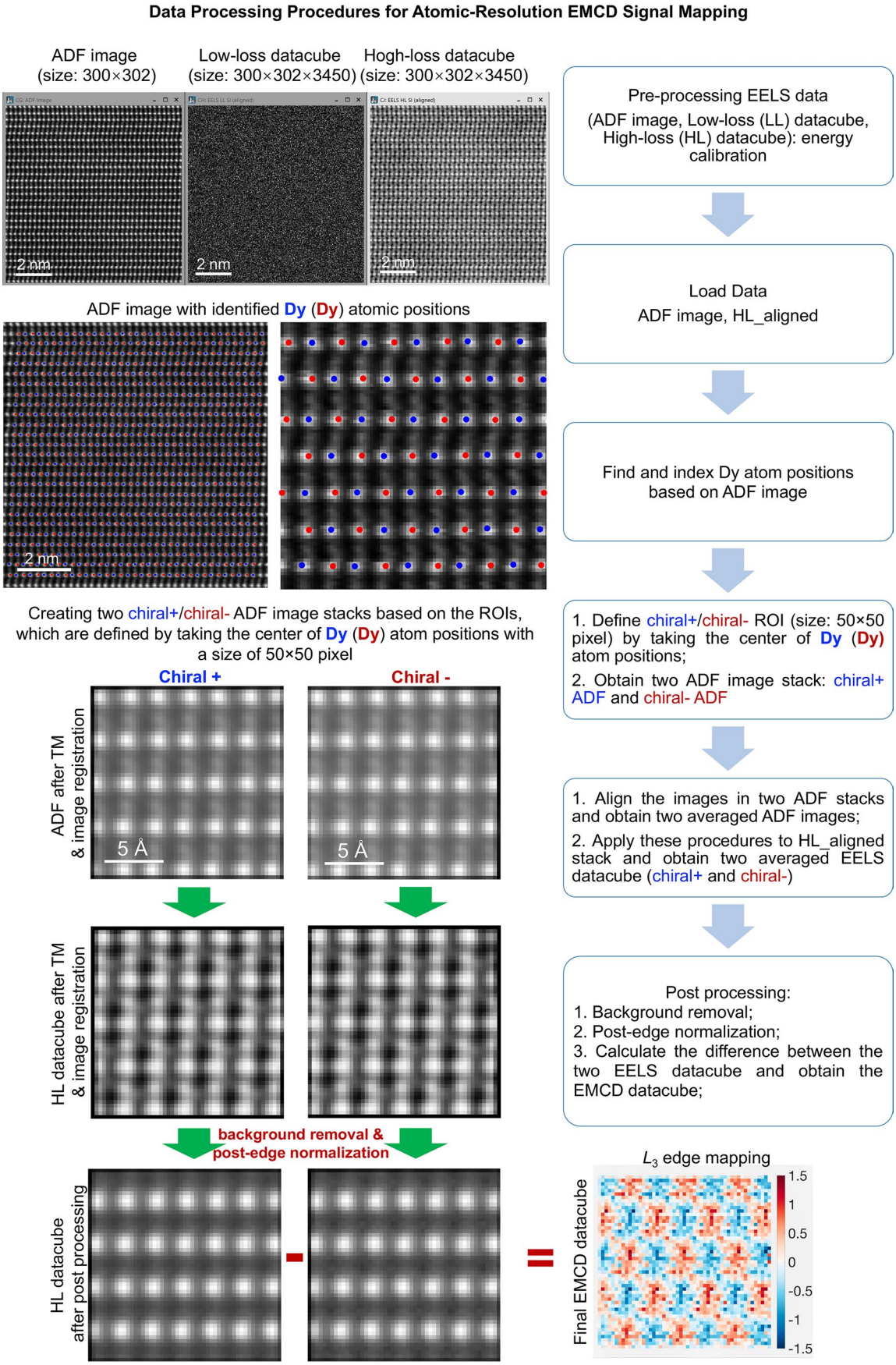

Extended Data Fig. 5 | See next page for caption.

https://doi.org/10.1038/s41565-026-02134-z

Extended Data Fig. 5 | Data processing procedures for mapping atomic-column-by-atomic-column EMCD signals. (1) The STEM-EELS experiments generate the following data files: ADF image; low-loss EELS (LL); high-loss EELS (HL). An energy calibration is performed based on the LL data using Digital Micrograph software. (2) The ADF image is used to identify and fit the positions of the Dy atomic columns. The Dy columns are indexed with two colored dots, which serve as the centers of the regions of interest (ROIs) for the chiral+ and chiral- groups. An ROI size of 50 × 50 pixels is used for template matching. The ROIs are extracted and categorized into two groups: chiral+ and chiral-. (3) The chiral+ and chiral- groups of ADF stack images are aligned and averaged to produce two final ADF images. Template matching and non-rigid image registration are used to correct distortions and misalignments between the two stacks. (4) The same alignment procedures are applied to the HL data, yielding two chiral EELS datacubes with an improved signal-to-noise ratio. (5) Post-processing, including background removal and post-edge normalization, is performed on both chiral EELS datacubes to generate two processed HL stacks, in which the spectrum image of the Fe sublattice is shown using an energy integration window from 680 to 780 eV. The EMCD datacube is obtained by taking the difference between these two processed stacks.

https://doi.org/10.1038/s41565-026-02134-z

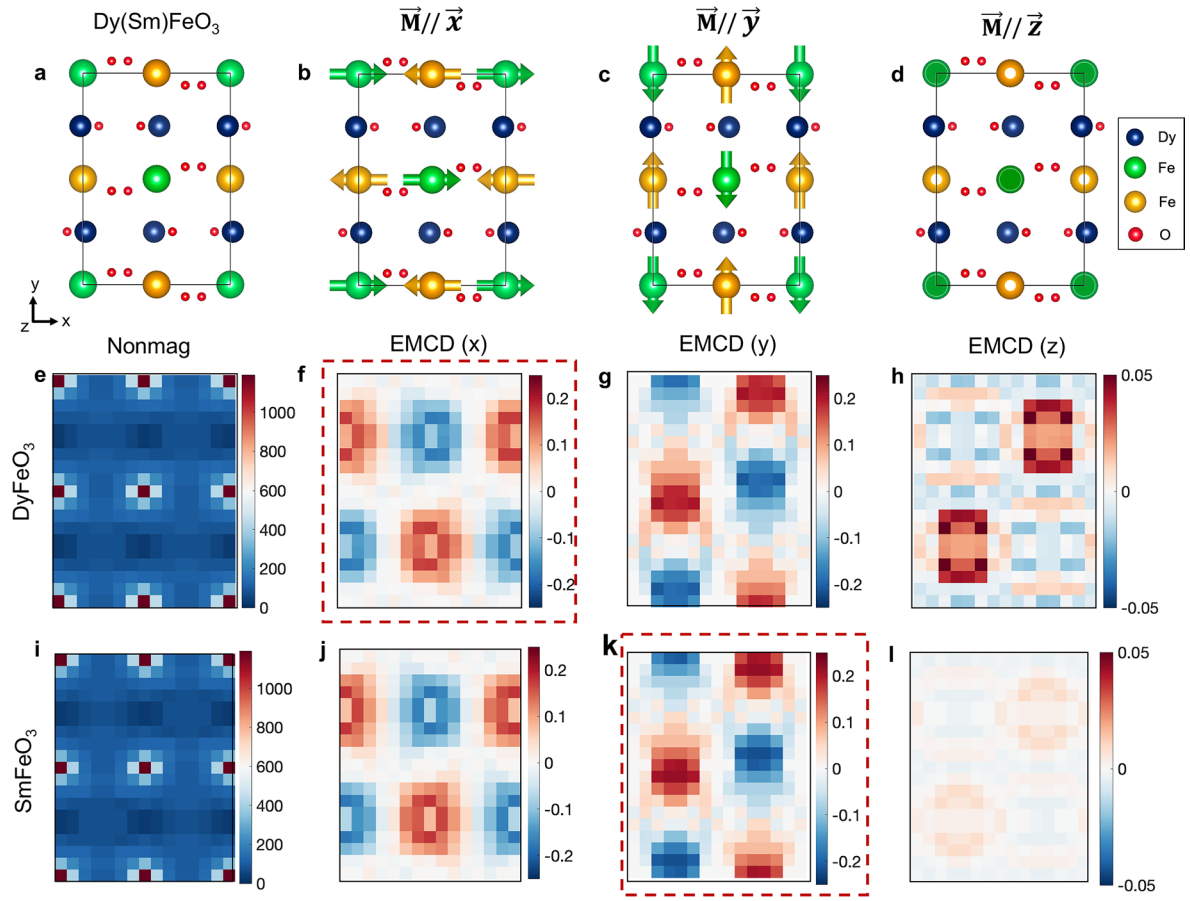

Extended Data Fig. 6 | Discussion of atomic-column-by-atomic-column EMCD measurements in three spatial directions. a, Atomic model of $DyFeO_3$ ($SmFeO_3$) projected along the *z* direction. **b-d**, Atomic model of $DyFeO_3$ ($SmFeO_3$) with Fe spins oriented along the *x*, *y* and *z* directions, respectively. **e,i**, Real space map of the simulated nonmagnetic signal across the unit cell. **f-h, j-l**, Real space maps of the simulated EMCD signals across the unit cell for $DyFeO_3$ and $SmFeO_3$, assuming that the magnetization is along the *x*, *y* and *z* directions, respectively. The actual spin orientations and corresponding EMCD maps are marked using dashed rectangles for $DyFeO_3$ in **f** and $SmFeO_3$ in **k**, respectively. The EMCD signals for the *x* direction are isolated from those for the *y* direction. The EMCD signals for the *x* and *y* directions can be distinguished by extracting signals from different regions in the STEM-EELS data. The EMCD signals for the *z* direction are almost negligible, due to the antisymmetric distribution of the signals in the diffraction plane. For most antiferromagnetic materials, the magnetic field required for spin flipping (*that is*, to reorient the magnetic vector in the direction of the external magnetic field) is much higher than the field applied by a fully-excited objective lens in the TEM (~ 2 T).

https://doi.org/10.1038/s41565-026-02134-z

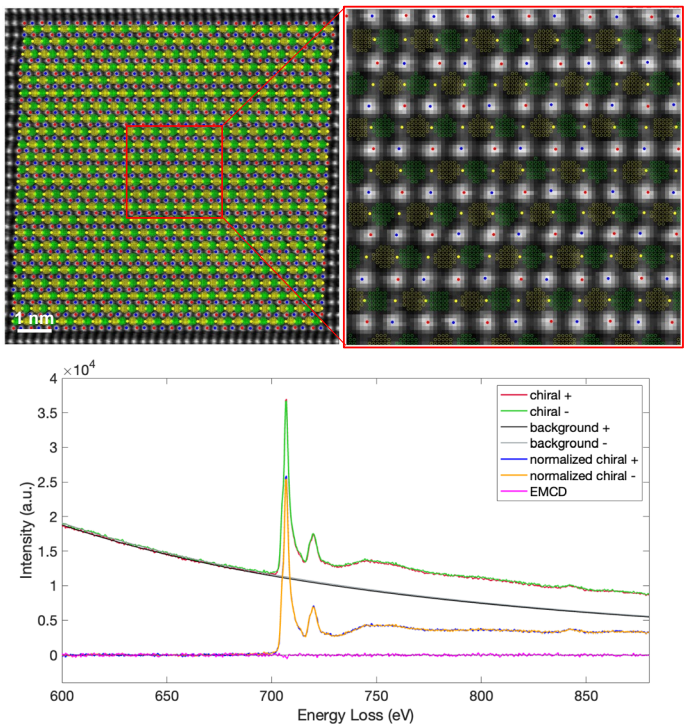

Extended Data Fig. 7 | Extraction of atomic EMCD signals from the y-component spin orientation contribution in $DyFeO_3$. The upper left panel shows the atomic columns fitted and indexed on the ADF image. The upper right panel shows a magnified region, on which regions of interest (ROIs) are marked for the chiral+ (green small circles) and chiral- (yellow small circles) positions, corresponding to the distributions of the EMCD signals in Extended Data Fig. 6c and Extended Data Fig. 6g when the spins are aligned along the *y*-axis. The lower panel shows the summed chiral EELS signals and the final EMCD signals. The negligible EMCD signals confirm that the magnetization is oriented along the *x* direction, as expected.

https://doi.org/10.1038/s41565-026-02134-z

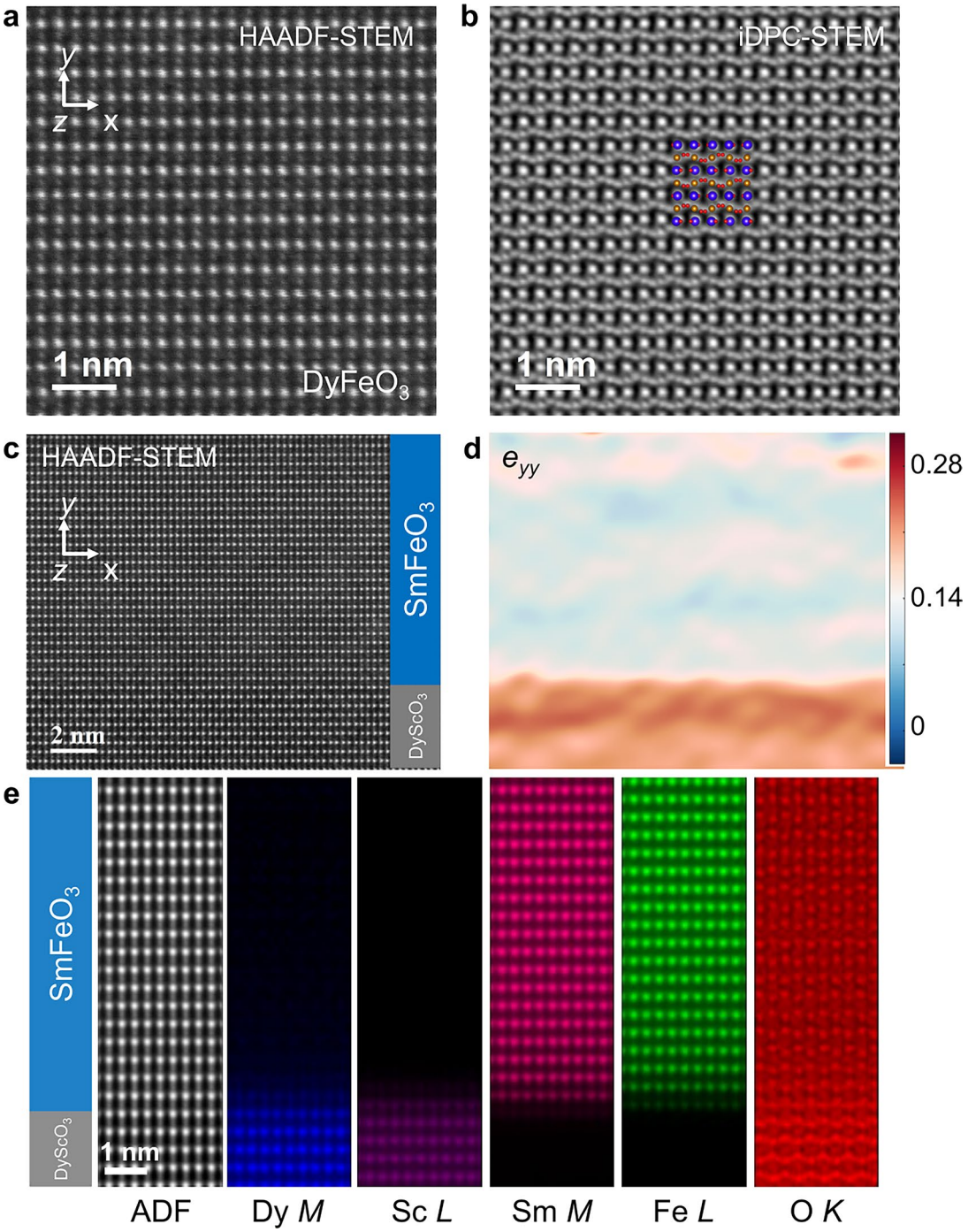

Extended Data Fig. 8 | Atomic-resolution images of a $DyFeO_3$ crystal and a $DyScO_3$-SmFeO3 interface used for atomic-column EMCD measurements. **a**,**b**, HAADF-STEM and iDPC-STEM images of the $DyFeO_3$ crystal along the *z*-axis, respectively, with overlaid atomic models. **c**, HAADF-STEM image of the $DyScO_3$-$SmFeO_3$ interface along the *z*-axis. The interface is not clearly identifiable due to the similar atomic numbers of Sm and Dy. **d**, The interface can be resolved by calculating the vertical strain e_{yy} using geometrical phase analysis (GPA). **e**, Elemental maps of Dy, Sc, Sm, Fe and O across the interface.

https://doi.org/10.1038/s41565-026-02134-z

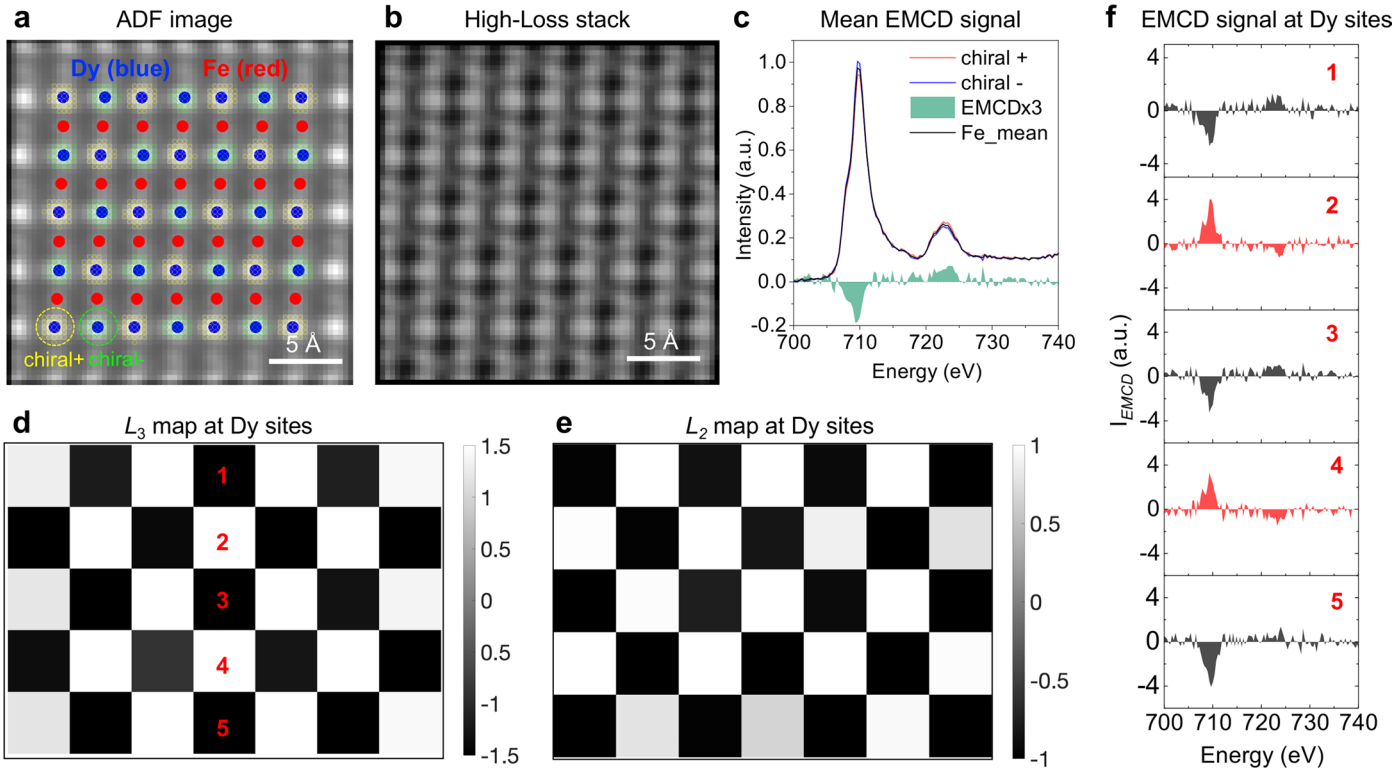

Extended Data Fig. 9 | Extraction of EMCD signals for $DyFeO_3$ without applying the half-unit-cell shift described in Extended Data Fig. 5. a, ADF image after template matching. The Dy (blue) and Fe (red) atomic columns are marked with corresponding colored dots. The chiral+ and chiral- regions used for chiral EELS signal extraction are indicated by yellow and green circles, respectively. **b**, The corresponding EELS stack after template matching. **c**, The chiral + , chiral- and mean EELS signals. **d,e**, EMCD maps at the L_3 and L_2 edges obtained by comparing the EELS signals at the Dy sites with the mean Fe L-edge spectrum. **f**, Representative EMCD signals from five selected Dy sites, as indicated in **d**.